

STRAIN-BASED DAMAGE ASSESSMENT OF STIFFENED COMPOSITE PANELS FOR STRUCTURAL HEALTH MONITORING PURPOSES

DIMITRIOS P. MILANOSKI AND THEODOROS H. LOUTAS

Laboratory of Applied Mechanics and Vibrations
Dept. of Mechanical Engineering and Aeronautics, University of Patras
Patras University Campus, GR-26504, Rio-Patras, Greece
e-mail: d.milanoski@g.upatras.gr; thloutas@upatras.gr

Key words: Parametric finite element model, Composite stiffened panel, Structural health monitoring, Fiber Bragg gratings, Non-linear buckling analysis.

Abstract. A common defect of composite stiffened panel structures is the disbond at the interface between the two constituents (skin/stringer), as a result of inefficient manufacturing process or foreign object impacts in service. Generally, discontinuities within the volume of an elastic solid media subjected to mechanical load, cause anomalies on the strain field in the near vicinity of the discontinuity. Utilizing this observation, the current work investigates the effect of artificially induced disbonds between skin/stiffener at a co-cured CFRP/epoxy single-stiffener generic element. A structural health monitoring methodology is developed, leveraging on numerically simulated strains along the stringer foot which aims to assess the health state of the sensorized structure as compared with a pristine baseline. The study is implemented with a parametric finite element model generating various disbanded cases. Longitudinal strain values are acquired at the exact points where in reality actual Fiber Bragg Grating sensors will be located.

1 INTRODUCTION

Primary airframe structures made of composites tend to increasingly replace more conventional materials. Their advantages correlate to the high specific mechanical properties over metallic materials. Nevertheless, these materials suffer from hidden damages, such delaminations/disbonds which arise major concerns if not identified at an early stage. In this direction, researchers utilize Structural Health Monitoring technologies to identify and assess damage. Fiber optic sensors (FOS) technology has gained increasing popularity as an alternative method of real-time strain measurements during structural service with minimum additive weight. A popular category of FOS are fiber Bragg grating sensors (FBGs) [1]. Quite a few researchers developed health monitoring methodologies like Li et al. [2], who proposed an automated algorithm based on static strain FBG readings on naval composite T-joints. A baseline of the pristine specimen was developed through which disbond cases were qualitatively

detected. A new method to identify strain modification along disbonds, exploiting Artificial Neural Networks (ANNs), was proposed by Kesavan and co-authors on the aforementioned specimens [3]. Takeda et al. [4] investigated interlaminar damage occurred by low-velocity impacts on CFRP stiffened panels. They used embedded FBGs to monitor the reflection spectra using the central wavelength of the sensors. A framework utilizing FBG strain readings was proposed by Airoidi et al. [5]. The authors developed an integrated Health and Usage Monitoring System (HUMS) of composite spars belong to wing-box, aiming to monitor both load and damage. A study based on static strains obtained by closely placed optical fibers with FBGs, was implemented in [6]. In this case, the differential strain of closely attached sensors placed away from damage, maintained a linear relation with respect to a reference strain, while sensors closest to damage showed a non-linear behavior. Sbarufatti et al. [7] followed a model-based methodology leveraging on a global-local finite element model of a helicopter tail boom in order to evaluate real fatigue crack propagation events. Damage detection was enabled by utilizing the Mahalanobis distance, considering a damage index calculated at each sensor. The methodology was validated experimentally using permanently placed FBGs to record strain data. Finally, a parametric numerical model was created by Zarouchas and Alderliesten [8] to evaluate the damage tolerance capabilities of aluminum stiffened panels. A non-linear buckling analysis was applied, and critical stability aspects of the panel regarding the disbond characteristics, i.e. position and size were highlighted.

The objective of the present paper is to study the effect of disbonds in the strain-field developed on the feet of single-stiffener panels (SSPs) and propose strain-based Health Indicators (HIs) capable of identifying and monitoring structural damage and specifically skin/stringer disbonding. Parametric numerical modeling is implemented to this direction.

2 NUMERICAL ANALYSIS

The numerical modeling procedure is presented in the following. First, the SSP specimen is introduced and its geometrical characteristics are detailed. The test article is consisting of two individual parts, a thin composite flat plate, the skin, and a composite T-section stiffening beam, called i.e. the stringer. The present study investigates the distribution of longitudinal static strains on the outer surface of each stringer foot in health and defected scenarios. The main objective of this work is to utilize the baseline and the strain alterations caused by skin/stiffener disbond and propose suitable HIs to assess/monitor the health state of the structure. The interrogation points are selected in a manner to simulate permanently installed optical fiber sensors, with Bragg gratings in pre-selected locations. Initially, strains from the pristine (healthy) SSP are obtained. Then, a parametric finite element model is created, simulating several disbond cases, in order to assist the objective of this study. Further details regarding the parameterized way of modeling are given below.

2.1 Single-Stiffener Panel configuration

The geometrical dimensions of the SSP, expressed in *mm* are provided in Figure 1, accompanied by the stacking sequences of each member. The material used in this study is an IM7/8552 carbon/epoxy unidirectional continuum fiber-reinforced prepreg, with nominal cured

ply thickness 0.131 mm [9] and mechanical properties [10] as detailed in Table 1. From a numerical analysis point of view, the final geometry of the two members is modelled considering a co-bonding manufacturing technique, without adhesive film in the interfacial region.

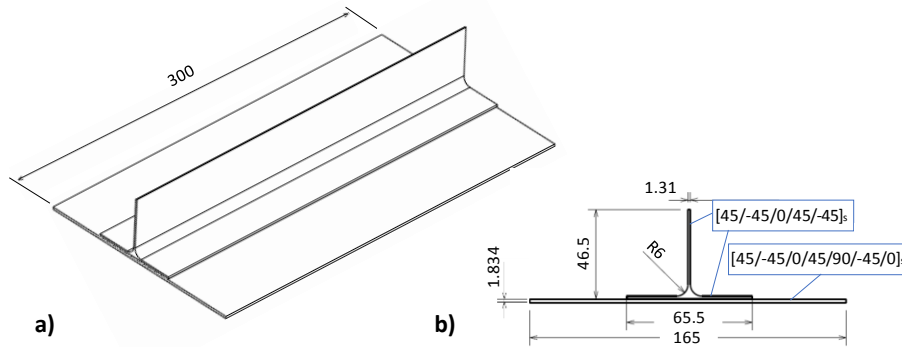


Figure 1: Dimensions of SSP specimen, a) perspective and b) cross-sectional view

Table 1: Engineering and interlaminar properties of IM7/8552 [10]

E_{11} (GPa)	E_{22} (GPa)	G_{12} (GPa)	ν_{12}	G_{Ic} (N/mm)	G_{IIc} (N/mm)	η (-)
150	9.08	5.29	0.32	0.277	0.788	1.6

2.2 Finite Element Model

The numerical model created, simulates the quasi-static compression of the pre-defined SSP. The SSP is loaded under displacement control, in an attempt to simulate the real test procedure. Cast-tab pots are used as load/support members to uniformly transmit the load to the specimen. Hence, two 30 mm exterior regions on the longitudinal direction bind to the pots. A schematic illustration of the test article is showed in Figure 2, indicating also the two SMARTapes[®] accommodating the optical fibers with FBGs (provided by SMARTEC-Switzerland) and the respective sensor spacing. These tapes are made of GFRP/epoxy and protect the accommodating optical fibers from harsh environmental conditions. The global coordinate system (XYZ) of the model is located at the symmetry plane of the top loading tab. Also, a local system (xyz) is defined at the start of each SMARTape[®] (one illustrated in Figure 2). Results regarding disbonds underneath this region will be expressed at the local coordinate system, as shown in Chapter 3.

The numerical study was implemented using the commercial finite element code Abaqus/Standard[®] [11]. Both members are modelled as one discrete layer of 4-node quadrilateral shell elements with reduced integration (S4R) and three integration points along the thickness. Every layer of composite laminates was modelled as a transverse isotropic material, according to the properties presented at Table 1, with thickness equal to the cured ply thickness the material provider suggests i.e. 0.131 mm. Earlier experimental works highlighted that degradation of the material properties is negligible in the early post-buckling region [12]. Thus, for the numerical modeling tasks associated with the present study, progressive

degradation of the material properties and intralaminar damage initiation/evolution were neglected. Instead of explicitly modeling the tabs, equivalent boundary conditions (BCs) have been imposed to the associated SSP partitions. On the support tab region, all six nodal degrees of freedom have been restrained, while on the loading one, the only degree set free is the spatial displacement U_z . Displacement control condition was applied on the loading tab region. Also, the filler region between the two radii (Figure 1b) was omitted in the modeling. Among the individual constituents i.e. the skin and the stringer, tie constraints were applied to their surfaces to guarantee common interface degrees of freedom and thus common kinematics. Regarding the strain interrogation points, each FBG numerically represented by a row of nodes with overall 10 mm length, as the common FBGs. Thus, ten node sets were created mimicking the actual FBGs. In every location where the FBG sensor is designed to be placed, the average strain of the contained nodes is extracted and assumed as the strain reading of each sensor. Two important observations are highlighted. First, in real conditions the SMARTape[®] is adhesively bonded in each foot and that might affect the strain readings. Second, the strains are extrapolated by the ambient elements to each (FBG) node.

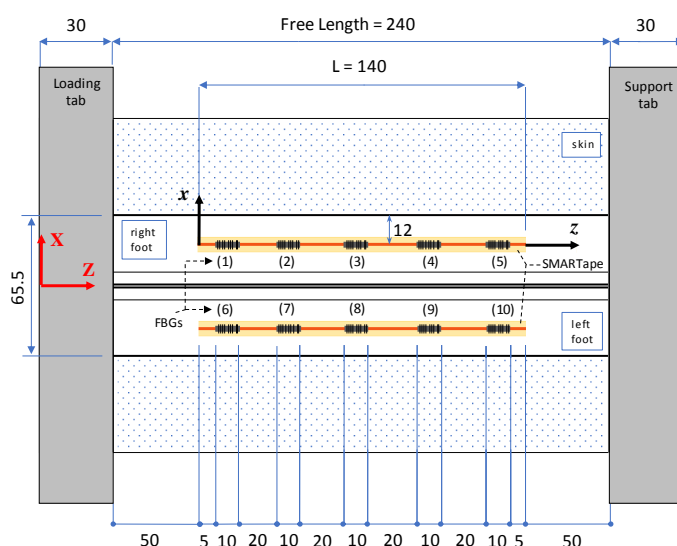


Figure 2: Conceptual design of sensorized specimen

The numerical analysis is divided in two steps, as (buckling) instability issues arise under these load conditions. Initially, a linear buckling analysis is executed for the estimation of the buckling (eigen)modes and associated eigenvalues. A compressive unit load is applied which means that the eigenvalues express the critical buckling load with respect to the corresponding mode. Since linear perturbation analysis is not predicting stresses and strains but rather a normalized displacement field of the structure, a non-linear buckling analysis is compulsory. An important role is played by appropriate imperfections acting as triggering mechanism for the buckling initiation (bifurcation point). In general, two main categories of imperfections are considered in the literature [8] and described as:

- Normalized nodal displacements obtained via linear buckling analysis are

introduced in the imminent non-linear analysis, following the pattern of the considering buckling modes

- A constant, low amplitude force acting along the buckling direction

The second method can alter the strain field in the adjacent region of the actuation point, while the second represents a more sensible way to model the buckling behavior. In the present study, the first way of introducing imperfections is chosen, especially due to the need to obtain as much as possible reliable strain estimations. These imperfections in general are defined by superimposing multiple eigenmodes, and have the following amplitude form with respect to the global coordinate system:

$$\Delta x_i = \sum_{i=1}^n w_i \varphi_i \quad (1)$$

where w_i is the scale factor correlated with the i -th mode shape φ_i . Only the 1st buckling mode was introduced as the lowest modes are frequently more critical, and a scale factor equal to 10% of the stiffener thickness was used. A static Newton-Raphson (N-R) solver, incorporating non-linear geometry formulation was utilized to solve the equilibrium of the non-linear problem. A maximum displacement equal to 0.25 mm was set for loading BC, as deep post-buckling analysis was not relevant with the current study. Due to such excitation, buckling occurred and characterized by the non-linear relation between the reaction force and displacement of the panel. Also, the maximum lateral deflection of skin midplane reached 4.7 mm. So, as buckling load considered the limit load where the linear load-displacement relation is maintained. A mesh convergence study was implemented, regarding the buckling load as this was obtained from both linear and non-linear analysis.

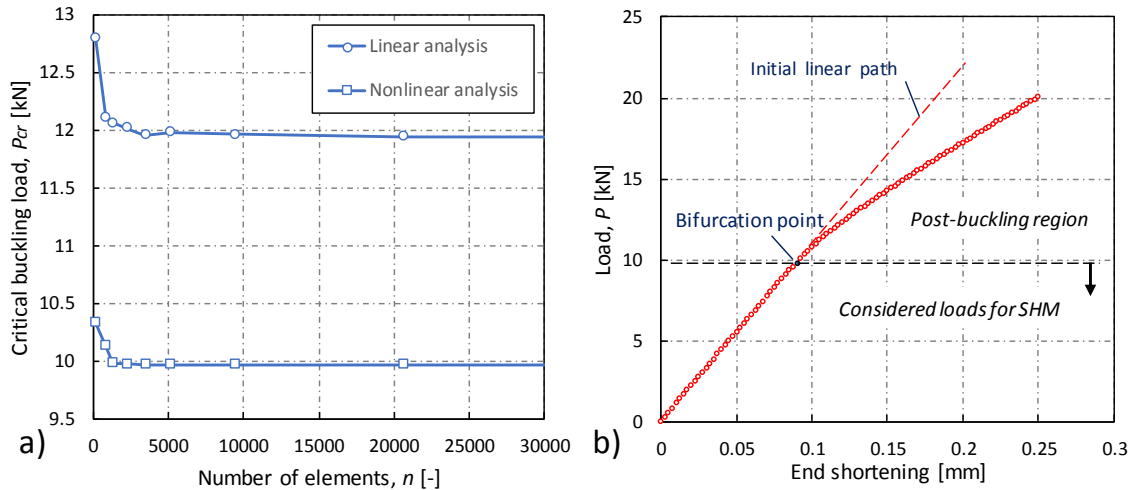


Figure 3: a) Mesh convergence and b) load-displacement curve for considered mesh density

The relevant results are depicted in Figure 3 and the load-displacement curve of the chosen mesh density is illustrated in Figure 3. Convergence was achieved in much lower number of elements, but in order to increase the fidelity of the model, an approximate element size of 2.00

mm was selected producing a total discretization of 20550 elements, as shown in Figure 4. Implementation of the Virtual Crack Closure Technique (VCCT) [13] also requires refined (global) mesh configurations or local refinement.

2.3 Parametric Analysis

The next task deals with the development of a parametric finite element model of the SSP with an artificially induced skin/stiffener, rectangle disbond. The parameterization concerns the position and the size of the disbond assuming a constant width along the right foot, as shown in Figure 4. In order to generate repetitive disbond scenarios at the skin/stiffener interface, a script written in Python[®] [14] was elaborated. The advantage of this method was the easy applicability, while the script was executed directly via the interface of Abaqus[®]. Most importantly, all manual tasks regarding the modeling using Graphical User Interface (GUI) of Abaqus[®] could be expressed in Python[®] language using proper libraries of the program. So, the script was created on the basis of iteratively generate the geometry, including the parametric position and size of the disbond, while it entailed all of the rest of the model attributes, as these have been previously described (material properties, mesh, BCs, etc.).

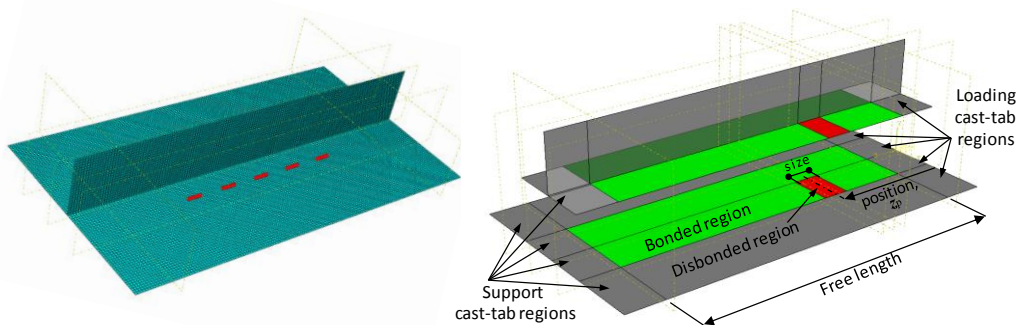


Figure 4: a) Discretized SSP, highlighting the right-foot FBG set, b) partitions of SSP

As we described previously, tie constraints were introduced at the interface region between the skin and the stiffener. Modeling the disbond was achieved by erasing that interaction and allow each of the individual regions of the disbond to freely move, without any kinematic constraint imposed by the other. The specimen was divided in partitions, in a manner of ensuring that coincident nodes at the interface of the two parts were generated. This approach prevented excessive distortion of the elements at the interface while it also allowed the correct implementation of the VCCT, in interfacial disbond propagation case studies. In current analysis, the VCCT was also used in order to assess if the disbonded regions do propagate under the defined loading condition. The interlaminar fracture properties of the IM7/8552 were used according to Table 1. Note that the VCCT is implemented by replacing the tie constraints with a contact interaction. This technique numerically calculates in every step the strain energy-release rate in a pre-defined crack/disbond front. For given critical strain energy-release rates of the material, the B-K criterion [15] controls the fracture initiation and allows the front

elements to separate if the criterion is satisfied. Also, the VCCT implementation requires to explicitly determine the unbonded region nodes in order to evaluate the strain energy release rate along the formed disbond fronts. This was also taken into consideration in the written script, so we can indicate the node sets that were created per iteration as:

- one node set, representing the bonded region, unique for every pair of disbond position and size
- ten node sets, representing the FBGs along each foot, unique for all pairs of disbond position and size

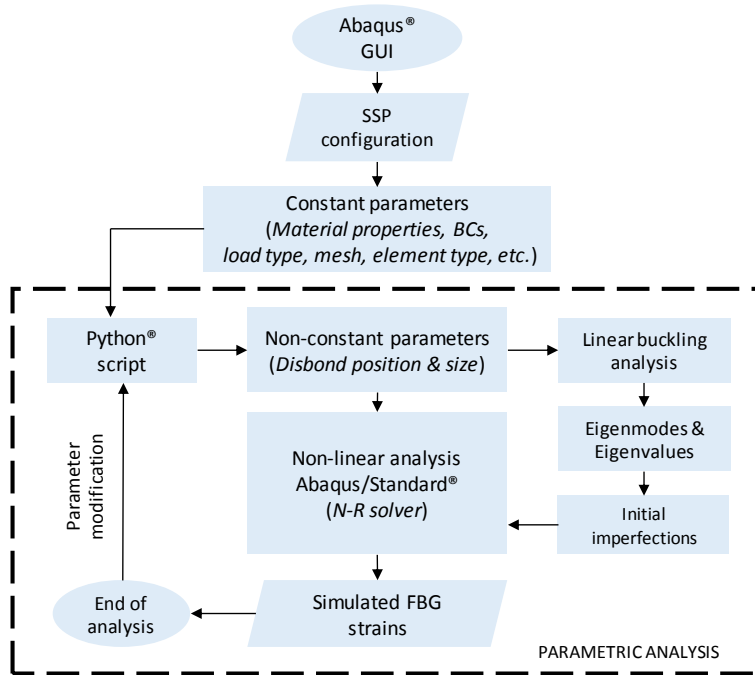


Figure 5: Explanation flow chart of the parametric analysis

None of the considered analyses showed propagation of the associated disbond. Generally, if it is ensured that fracture procedures are not involved, simple tie constrains can be utilized at the bonded region of the two members over the VCCT. A detailed flow chart describing the parametric implementation of the present work, is shown in Figure 5. After completion of every iteration, the disbond characteristics were updated, regarding either the position or the size.

3. DAMAGE ASSESSMENT OF SKIN-TO-STIFFENER DISBOND

In the current section, the effectiveness of two Health Indicators (HIs) on the detection of numerically simulated skin/stiffener disbonds will be investigated. The strain data obtained from the pristine specimen are considered as the baseline. Next, a SHM methodology based on the results obtained by the parametric analyses of skin-to-stiffener disbonds was evaluated. As mentioned before, the parametric analysis generates models with disbond in the interface of skin/stiffener, beneath the right foot. The assessment of disbond cases, within the assumed sensor topology, initiated by introducing a health indicator to estimate the sensitivity of the

FBGs to the disbond position. Finally, the behavior of a second health indicator was investigated versus the disbond size.

3.1 Baseline SHM Methodology

The static strains obtained from the pristine specimen after the non-linear analysis, establish the healthy-baseline which is utilized to reveal the presence of disbonds. Only strains prior to buckling, that belong to the linear portion of load-displacement curve are considered. Furthermore, regarding the disbond cases, similar data are gathered and stored, for each individual disbond scenario. The strains of every FBG are simulated for several load values as different displacements are imposed. Small discrepancies between the strains at the two feet are observed, mainly for the two FBGs closest to the loading tab. The presence of an interfacial disbond region, affects the strain distribution along the foot. An arbitrary case of disbond at position $z_p = 60 \text{ mm}$, and three different sizes, is depicted in Figure 6, under a constant static compressive load of 6.0 kN. The strain perturbation induced by the disbond can be clearly noticed in the vicinity of its edges. The gradient in those regions abruptly increases and the deviation from the pristine (dashed line) distribution is highlighted. The left (fully-bonded) foot shows no deviation from the baseline. Also, the marked points that illustrate FBG readings are highlighted along the curves. Generally, the difference between the strain reading of each FBG for disbonded case and the baseline i.e. the differential strain, shows an increasing trend proportional to the load. The most affected FBG shows higher discrepancies and is linearly increasing up to buckling load, as shown in Figure 6. Hence, a notable remark is extracted as the rest of the FBGs show almost negligible deviation from the baseline up to the buckling load. As the disbond changes position along the foot, a similar pattern of the strain discrepancy was obtained following the disbond position (not shown here). Moreover, the gradient and the amplitude of the discontinuity is not maintained constant and exhibits dependency both on position and load.

In order to estimate the impact of the disbond position to strain modification, a Health Indicator (HI) will be utilized based on the relative strain differences of each FBG in an arbitrary condition with the baseline. The HI is a metric of the strain change, under the same load amplitudes and is calculated as shown in eq. (2).

$$HI_i^1 = \left(\frac{|\varepsilon_{11}^{pristine} - \varepsilon_{11}^{disb}|}{\varepsilon_{11}^{pristine}} \right)_i, i = 1, 2, \dots, 10 \quad (2)$$

where i corresponds to the FBG number. To see the effect of changing external load, an average value of the HI with changing load can be simply calculated, considering n total load cases:

$$\overline{HI} = \frac{1}{n} \sum_1^n HI_i^1, i = 1, 2, \dots, 10 \quad (3)$$

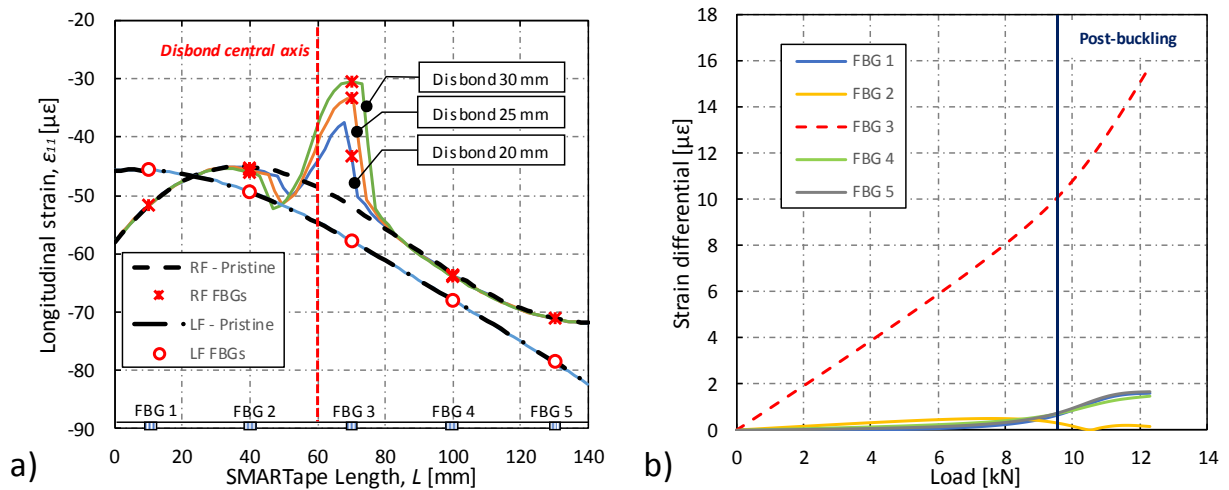


Figure 6: a) Simulated strain distributions along left (LF) and right (RF) foot, associated with disbond cases and b) differential strain over load on RF for 20mm disbond case

Assuming a constant disbond size of 20 mm, the HI indices of the FBGs located at the right foot ($i = 1, 2, 3, 4, 5$) are calculated. Through the parametric numerical model, disbonds in several positions in a range 10-130 mm regarding the local coordinate system (xyz) are created. The disbond position is incrementally increasing by 5 mm. The average HI is calculated for every FBG, and the results versus the disbond position are depicted in Figure 7. HI values above 2% are obtained by the current sensor topology, to almost every position of the disbond along the foot. It can be noticed that lower discrepancies occur when a sensor is placed at central position along the disbond against the cases that a sensor is above the disbond front. This estimation can be evaluated by noticing the strain discontinuity profile as it is shown in Figure 6.

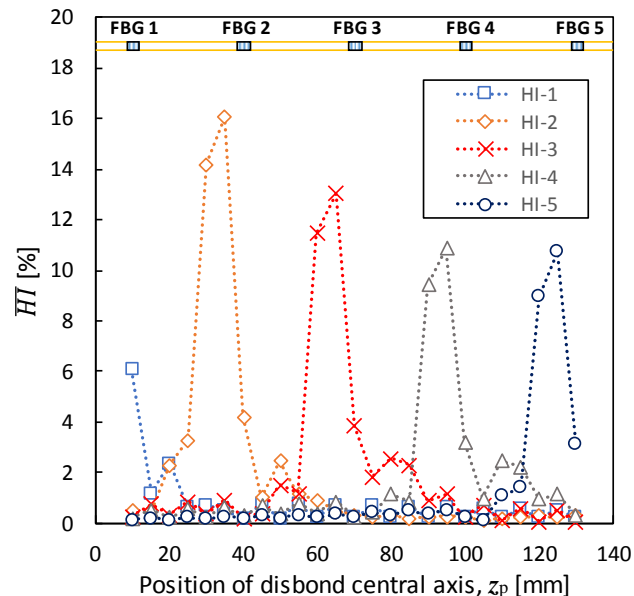


Figure 7: Health indicator predicted by each FBG versus the disbond position along RF

Next, we introduce a second HI fit for Structural Health Monitoring, while the disbond is increasing. This HI combines the strain readings from all sensors. In fact, it represents the percentage each FBG sensor holds of the cumulative strain among the five FBG sensors, and is defined as:

$$HI_i^2 = \varepsilon_i^N = \frac{\varepsilon_{11}^i}{\sum_i \varepsilon_{11}^i}, \text{ for RF: } i = 1, \dots, 5 \text{ and for LF: } i = 6, \dots, 10 \quad (4)$$

where again i corresponds to FBG numbering. This HI is inspired by the observation that the strain of the unaffected sensors shows minor deviation from the healthy condition. In Figure 8a the average values of the HI for every FBG are presented, indicating first the pristine values accompanied by several disbond size cases. The central axis of the growing disbond is at $z_p = 60 \text{ mm}$, as mentioned before and the disbond is assumed to grow by the same length from each side. Finally, in Figure 8b the HI is presented for every FBG under increasing size of disbond. The 3rd sensor on the RF is the most affected by the disbond front and this fact is illustrated with a monotonical drop on its index of about 8% regarding the intact specimen value. The rest FBG sensors show a slight increase of their HI values, no more than 2%. Only the 2nd sensor shows an increase higher than 2% in the case of 50 mm disbond as the disbond front reaches this sensor too.

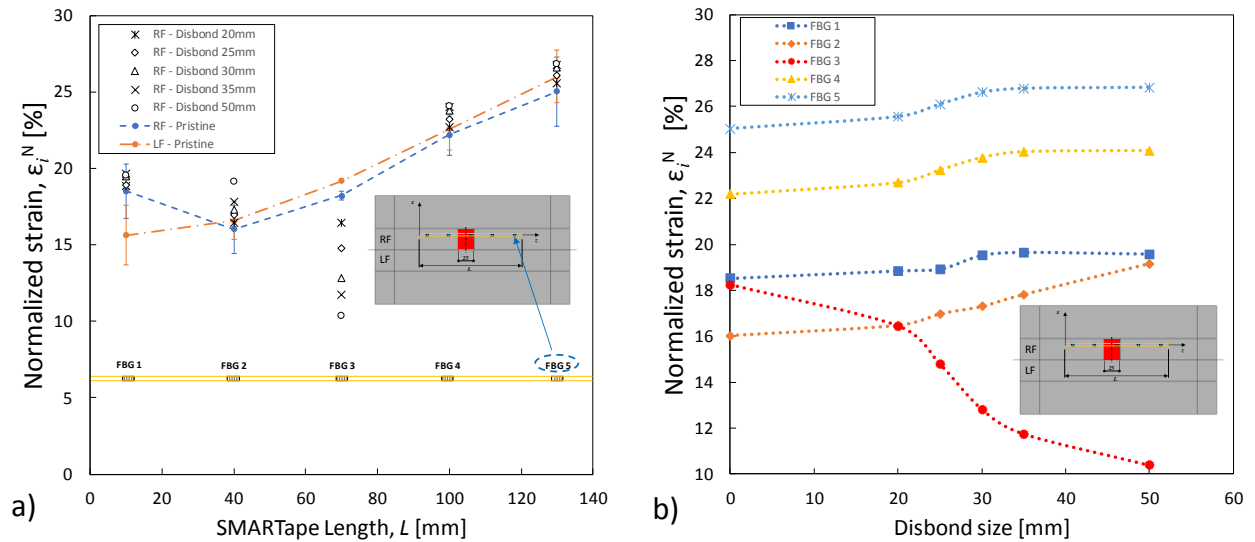


Figure 8: a) Normalized strain indices of FBGs on pristine and various disbonded specimens and b) gradual change of indices versus an increasing disbond size

4 CONCLUSIONS

In the current study, a model-based methodology for damage assessment on generic single-stiffener composite panels was approached. Towards that end, a finite element analysis was conducted in order to simulate the composite panel subjected to uniaxial compressive

loading. Longitudinal strains were computed at predefined regions where permanent FBG sensors will be attached. Initially, a non-linear buckling analysis was executed deriving the investigated strains on pristine (healthy) structure. Furthermore, numerous skin-to-stiffener disbonds were introduced via a parametric numerical model using Python® scripting.

First, by a strain differential methodology, the impact of the disbond positioning to the strain distribution was evaluated. For that purpose, a health indicator was used comparing longitudinal strains of the pristine baseline with the disbanded cases. Then, another indicator representing a strain normalization scheme of every sensor was calculated. The aforementioned index was illustrated for several disbond sizes and indicated a monotonic drop on the sensor that was more affected by the disbond. Conclusively, the first health indicator utilizes strains from the pristine baseline and those out of disbanded cases. It can be characterized as baseline-dependent. A drawback of this indicator lies on its load dependency, whilst a very interesting outcome is the small scatter that the indicator showed in the whole load range they were examined. On the other hand, the second indicator does not rely on baseline data. From that perspective and from the monotonic behavior it exhibits for increasing disbond size, it constitutes a promising choice for SHM.

ACKNOWLEDGEMENTS

The work presented in this paper was financially supported by the European Union's Horizon 2020 research and innovation programme ReMAP (Grant Agreement Number:769288). The support is appreciated by the authors.

REFERENCES

- [1] Güemes, A., Fernández-López, A. and Soller, B. Optical Fiber Distributed Sensing - Physical Principles and Applications. *Structural Health Monitoring* (2010) 9(3):233-245.
- [2] Li, H.C.H., Herszberg, I. and Mouritz, A.P. Automated Characterization of Structural Disbonds by Statistical Examination of Bond-line Strain Distribution. *Structural Health Monitoring* (2006) 5(1):83-94.
- [3] Kesavan, A., Sabu, J. and Herszberg, I. Strain-based Structural Health Monitoring of Complex Composite Structures. *Structural Health Monitoring* (2008) 7(3):203-213.
- [4] Takeda, S.-i., Aoki, Y. and Nagao, Y. Damage monitoring of CFRP stiffened panels under compressive load using FBG sensors. *Composite Structures* (2012) 94(3):813-819.
- [5] Airoidi, A., Bettini, P., Loutas, T., Koimtzoglou, C. and Sala, G. Design of health and usage monitoring systems based on optical fibers for composite wing spars. (2015) *28th ICAF Symposium*, Helsinki.

- [6] Fernández-López, A., Menendez, J.M. and Güemes, A. Damage Detection in a Stiffened Curved Plate by Measuring Differential Strains. (2007) *16th International Conference on Composite Materials*.
- [7] Sbarufatti, C., Corbetta, M., San Millan, J., Frovel, M., Stefaniuk, M. and Giglio, M. Model-assisted performance qualification of a distributed SHM system for fatigue crack detection on a helicopter tail boom. (2016) *8th European Workshop On Structural Health Monitoring (EWSHM)*, Bilbao, Spain.
- [8] Zarouchas, D.S. and Alderliesten, R.C. The effect of disbonds on stability aspects of adhesively bonded aluminum panels during compression loading. *Thin-Walled Structures* (2015) 96:372-382.
- [9] Hexcel Corporation, HexPly® 8552 Product Datasheet. (2016).
- [10] Bisagni, C., Vescovini, R. and Dávila, C.G. Assessment of the Damage Tolerance of Post-Buckled Hat-Stiffened Panels using Single Stringer Specimens. (2010) *51st AIAA/ASME/ASCE/AHS/ASC Structures, Structural Dynamics, and Materials Conference*.
- [11] Dassault Systèmes Simulia Corp, Abaqus Analysis User's Manual Guide. (2014) Providence, RI.
- [12] Dávila, C.G. and Bisagni, C. Fatigue life and damage tolerance of postbuckled composite stiffened structures with initial delamination. *Composite Structures* (2017) 161(1):73-84.
- [13] Krueger, R. Virtual crack closure technique: History, approach, and applications. *Appl. Mech. Rev* (2004) 57(2):109-143.
- [14] Python, Python Software Foundation (PSF), Python 3.7.0. (2018), *Wolfboro Falls, NH 03896-0037, PO Box 37*.
- [15] Kenane, M. and Benzeggagh, M.L. Mixed-mode delamination fracture toughness of unidirectional glass/epoxy composites under fatigue loading. *Composites Science and Technology* (1997) 57(5):597-605.